

Ultra-Broadband Strong Electromagnetic Interference Shielding with Ferromagnetic Graphene Quartz Fabric

Yadian Xie, Shan Liu, Kewen Huang, Bingbing Chen, Pengcheng Shi, Zhaolong Chen, Bingzhi Liu, Kaihui Liu, Zhiqiang Wu,* Ke Chen,* Yue Qi,* and Zhongfan Liu*

Flexible electromagnetic interference (EMI) shielding materials with ultrahigh shielding effectiveness (SE) are highly desirable for high-speed electronic devices to attenuate radiated emissions. For hindering interference of their internal or external EMI fields, however, a metallic enclosure suffers from relatively low SE, band-limited anti-EMI responses, poor corrosion resistance, and non-adaptability to the complex geometry of a given circuit. Here, a broadband, strong EMI shielding response fabric is demonstrated based on a highly structured ferromagnetic graphene quartz fiber (FGQF) via a modulation-doped chemical vapor deposition (CVD) growth process. The precise control of the graphitic N-doping configuration endows graphene coatings on specifically designable quartz fabric weave with both high conductivity (3906 S cm^{-1}) and high magnetic responsiveness (a saturation magnetization of $\approx 0.14 \text{ emu g}^{-1}$ under 300 K), thus attaining synergistic effect of EMI shielding and electromagnetic wave (EMW) absorption for broadband anti-EMI technology. The large-scale durable FGQF exhibits extraordinary EMI SE of $\approx 107 \text{ dB}$ over a broadband frequency (1–18 GHz), by configuring $\approx 20 \text{ nm}$ -thick graphene coatings on a millimeter-thick quartz fabric. This work enables the potential for development of an industrial-scale, flexible, lightweight, durable, and ultra-broadband strong shielding material in advanced applications of flexible anti-electronic reconnaissance, antiradiation, and stealthy technologies.

1. Introduction

Booming development of diverse electronic devices and wireless communication networks has brought electromagnetic interference (EMI) problems for the internal or external electronic components and the surrounding environment in an invisible and intangible way.^[1–6] The anti-EMI technology can efficiently prevent malfunctioning and performance deterioration of electronic devices, and reliably protect human health and surrounding environment, essential for the applications in electronic, automobile, aerospace fields, etc.^[7–9] Highly effective EMI shielding of material mainly relies on: 1) electromagnetic wave (EMW) reflection owing to surface free charge carriers interacting with EM fields; 2) EMW absorption based on electric and magnetic dipoles interacting with EM field, as well as the magnetic resonances and eddy currents from magnetic material; and 3) multiple internal reflections.^[10–12] Previously, metal and metallic composites are generally used as EMI shielding materials

Y. Xie, K. Huang, Z. Chen, B. Liu, K. Liu, Y. Qi, Z. Liu
Center for Nanochemistry
Beijing National Laboratory for Molecular Sciences
College of Chemistry and Molecular Engineering
Academy for Advanced Interdisciplinary Studies
Peking University
Beijing 100871, China
E-mail: qiyue-cnc@pku.edu.cn; zfliu@pku.edu.cn

Y. Xie, Y. Qi
Key Laboratory of Low-Dimensional Materials and Big Data
School of Chemistry and Chemical Engineering
Guizhou Minzu University
Guiyang 550025, China

Y. Xie, S. Liu, K. Huang, P. Shi, Z. Chen, B. Liu, K. Liu, K. Chen, Z. Liu
Beijing Graphene Institute (BGI)
Beijing 100095, P. R. China
E-mail: kchen@henu.edu.cn

B. Chen
School of Energy Science and Engineering
Nanjing Tech University
Nanjing 211816, China

K. Liu
State Key Laboratory for Mesoscopic Physics
Academy for Advanced Interdisciplinary Studies
School of Physics
Peking University
Beijing 100871, China

Z. Wu
Department of Electrical Engineering
Wright State University
Dayton, OH 45435, USA
E-mail: zhiqiang.wu@wright.edu

K. Chen
Center for the Physics of Low-Dimensional Materials
School of Physics and Electronics
Henan University
Kaifeng 475004, China

 The ORCID identification number(s) for the author(s) of this article can be found under <https://doi.org/10.1002/adma.202202982>.

DOI: 10.1002/adma.202202982

due to their notable EMI SE.^[13] Magnetic-nanoparticle-conducting polymer composites have been also investigated as conventional metal-alternative materials for EMI shielding and evinced a good performance.^[14] However, the inferiority of the above materials maximally constricts practical applications in the anti-EMI fields, mainly because of its heavyweight, band-limited responses, brittleness, and non-adaptability, as well as metal corrosion.

Carbon-based nanomaterials are expected to be one of the most potential substitutes for metal enclosures for EMI shielding because of their unique properties such as high electrical conductivity, corrosion resistance, and lightweight.^[15,16] Graphene, a 2D carbon layer, has naturally attracted much interest in this subject due to its excellent electronic and mechanical properties as well as highly accessible surface/interface.^[17–19] Most of the previously reported graphene materials (e.g., graphene films, graphene foams, graphene nanosheets, etc.) show the excellent reflection of electromagnetic waves, complying with the dominating EMI shielding mechanism for highly conductive materials.^[20,21] Nevertheless, such graphene shrouds exhibit limited SE, taking into account the weak ability of electromagnetic wave absorption of the thin carbon layers. The graphene-based materials are also reported to improve the microwave absorption ability for eliminating adverse electromagnetic waves. The graphene 3D interconnected network was constructed by using 2D graphene sheets and macroscopic 3D free-standing graphene foam showing the good microwave absorption performance. However, the drawbacks of unstable absorption, narrow absorption range, poor stability, and large loading content, have severely hindered their practical applications.^[14,21] To date, great efforts have identified that both hybridizing ferrites and doping heteroatoms into graphene lattice are the effective approaches to well match the characteristic impedance and induce the ferromagnetic (FM) moments for graphene-based shrouds,^[22–25] thus achieving high-performance EMI shielding.^[26] However, restricted by the properties of pristine graphene, previous study only took one of EMI shielding efficiency or bandwidth anti-EMI response into consideration, but so far is unable to be compatible with both key purposes simultaneously. An assembled macroscopic graphene shrouds with merits of both high conductivity and ferromagnetism targeting ultra-broadband strong anti-EMI technology have been elusive thus far.^[27–29]

In this work, $10 \times 0.5 \text{ m}^2$ flexible, highly conductive, and ferromagnetic graphene quartz fabrics (FGQF) with ultra-broadband strong EMI shielding effectiveness are prepared via a direct CVD system. Under a carefully designed growth strategy, the high-quality graphitic N-doped graphene can be successfully synthesized on the quartz fabric with the specific weaving structure by introducing carbon and nitrogen precursors into a continuous roll-to-roll CVD system. The highly conductive graphitic N-doped graphene layer ($\approx 3906 \text{ S cm}^{-1}$) exhibits the strong reflection ability of EMW. More importantly, graphitic N-substitutional doping in graphene lattice enables the modulation of localized magnetic ordering and FM, although the intrinsic graphene shows no ferromagnetism. First-principles calculations and magnetic measurements further indicate that N-substitutional level of $\approx 6.3 \text{ at\%}$ for graphitic N-doped graphene layers can induce a saturation magnetization as high as

$\approx 0.14 \text{ emu g}^{-1}$ under 300 K. In this way, the N-doped graphene layers are typically regarded as effective EMW absorbers.^[26] Such synergetic effect arising from excellent conductivity and ferromagnetism is beneficial for both EMI shielding and EMW absorption. Consequently, $\approx 2.3 \text{ }\mu\text{m}$ -thick FM graphene films show extremely high EMI SE of $\approx 58 \text{ dB}$. In particular, the FGQF at a thickness of merely $\approx 1 \text{ mm}$ exhibits extraordinary EMI SE of $\approx 107 \text{ dB}$ for anti-EMI technology responded over a broadband frequency (1–18 GHz) originating from the above synergetic effect, along with the unique multiple EMW reflections and multichannel absorption of EMW inside the fabric weave. Our work successfully developed an industrial-scale, flexible, lightweight, durable, and ultra-broadband strong shielding material in advanced applications of flexible anti-electronic reconnaissance, antiradiation, and stealthy technologies, also paves the way for the applications of 2D material-integrated fabrics in industry fields.

2. Results and Discussion

2.1. Growth of High-Quality Ferromagnetic Graphene on Quartz Fabric

High-crystallinity FM graphene coatings were grown on quartz fabric with the specific 5/2 satin and sateen weave structure. Figure 1a demonstrates FM graphene coatings on quartz fabric with a quasi-periodic structure of silica warp and weft weaves. The continuous batch production of FGQF is achieved based on a designable industrially implementable roll-to-roll CVD system at a controllable rolling speed from 0.05 to maximum of 0.2 m min^{-1} (Figure 1b). The full covering of graphitic N-doped graphene on the surface of quartz fabric is confirmed by scanning electron microscopy (SEM) observation of crossing sites of FGQF frameworks (Figure 1c,d), and the intact morphology of quartz fabric is well preserved. The representative Raman spectrum (Figure 1e) shows the sharp G- and 2D-mode peaks, indicating the high crystalline quality of the N-doped graphene coatings (the observable D peak is mainly attributed to the N doping and defective graphene domain boundaries). The X-ray photoelectron spectroscopy (XPS) analysis further confirms the presence of graphitic N-substitution in graphene lattices with the characteristic peak at 401.5 eV (Figure 1f, Figure S1, Supporting Information). The emergence of localized magnetic ordering and FM relies on graphitic-N doping in graphene lattices without introducing other types of defective N-doped sites. On scale-up, batch production of high-quality FGQF with tunable lengths up to 10 meters is successfully realized (Figure 1h, image of FGQF taken using an unmanned aerial vehicle (UAV), on the ground of a standard soccer field is supplied as an example). Unprecedentedly, the large-scale FGQF exhibits the ultrahigh EMI SE of 107 dB at the thickness of merely $\approx 1 \text{ mm}$ for anti-EMI technology responded over a broadband frequency (1–18 GHz), which outperforms that of other similar EMI materials (Figure 1g; Table S1, Supporting Information).

The tube-like graphene shell derived from a monofilament of FGQF overlaps into a ribbon with an average layer thickness of $\approx 2.0 \text{ nm}$ on the SiO_2/Si substrate after the removal of quartz fiber, as measured by SEM and atomic force microscopy

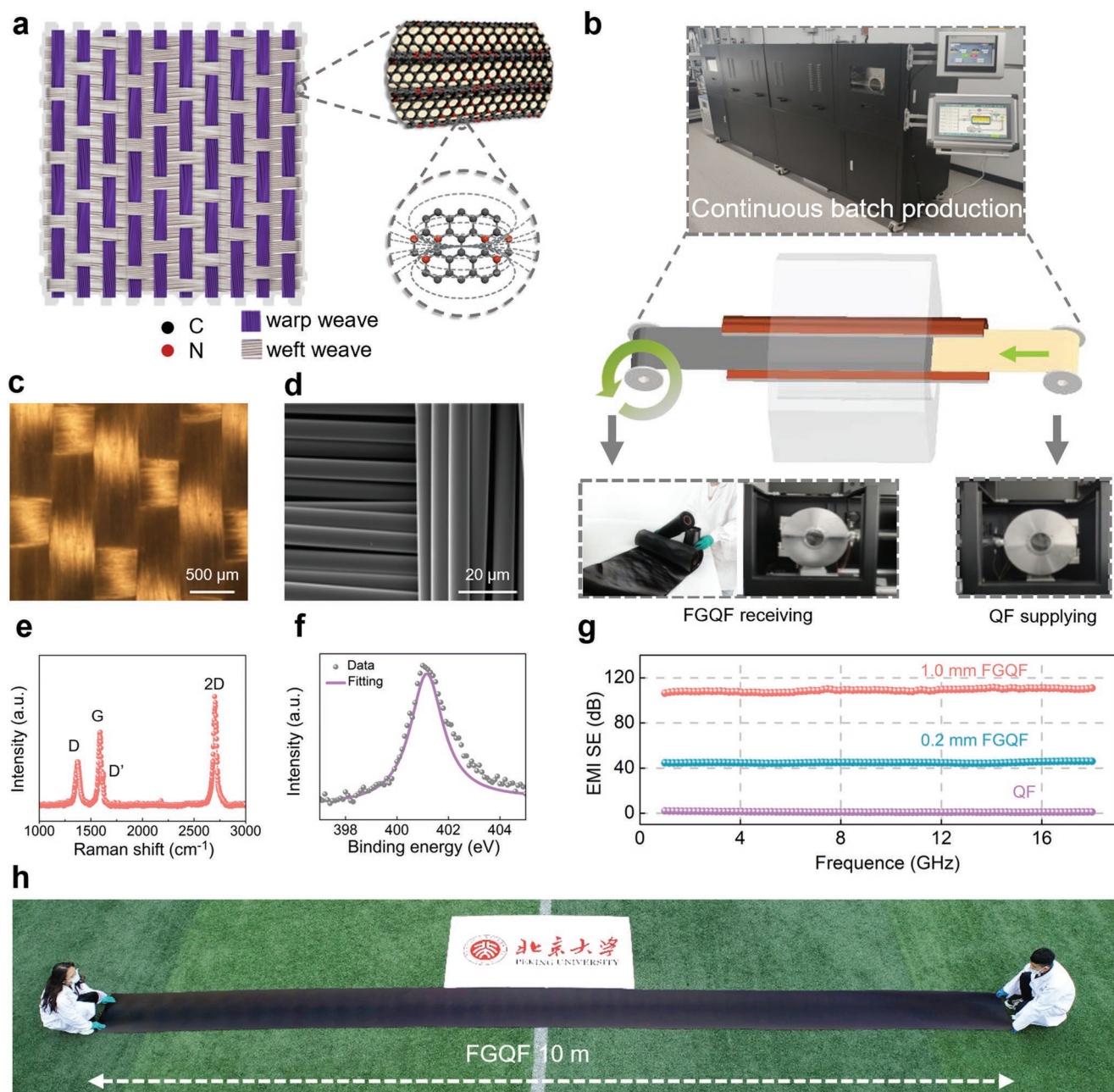


Figure 1. Growth and characterizations of FGQF. a) Schematics of FGQF. b) Continuous roll-to-roll CVD growth system for FGQF production. c,d) Optical and SEM images of 5/2 satin and sateen weave structure of FGQF. e) Raman spectrum of FM graphene on quartz fiber. f) Corresponding N 1s core-level XPS spectrum. A new peak at 401.5 eV occurs for the graphitic N-doped graphene. g) EMI SE of QF and FGQF with various thickness. h) Image of large-scale FGQF (10 × 0.5 m²) taken using an unmanned aerial vehicle (UAV), on the ground of a standard soccer field.

(AFM, Figure 2a,b). A high-resolution transmission electron microscopy (HRTEM) image of an individual graphene domain reveals the high crystallinity of the graphitic N-doped graphene (Figure 2c). Energy-dispersive spectroscopy mappings (EDS, Figure S2, Supporting Information) demonstrate the uniform distributions of C and N elements throughout the entire graphene layer on quartz fiber. As revealed by the Raman spectra (Figure 2d), the D peak strengthens while the 2D peak decreases with the increase of N content (max. 6.3 at% in this work), indicating that the N-doped or structural defects gradu-

ally increased, respectively. To further understand the graphitic N formation mechanism, the first-principles calculations are performed based on the experimental results. The formation energy of graphitic N-doped graphene on SiO₂ surface with a ≈6.3 at% N-doping level is only −2.48 eV, which is far less than that of pyrrolic (−0.64 eV) and pyridinic (−0.90 eV) N-doped graphene (Figure 2e). Further analysis of charge density difference and bader charge reveals the graphitic N atoms notably interact with Si atoms from the underlying substrates (Figure S3, Supporting Information). Thus, the charge transfer number is

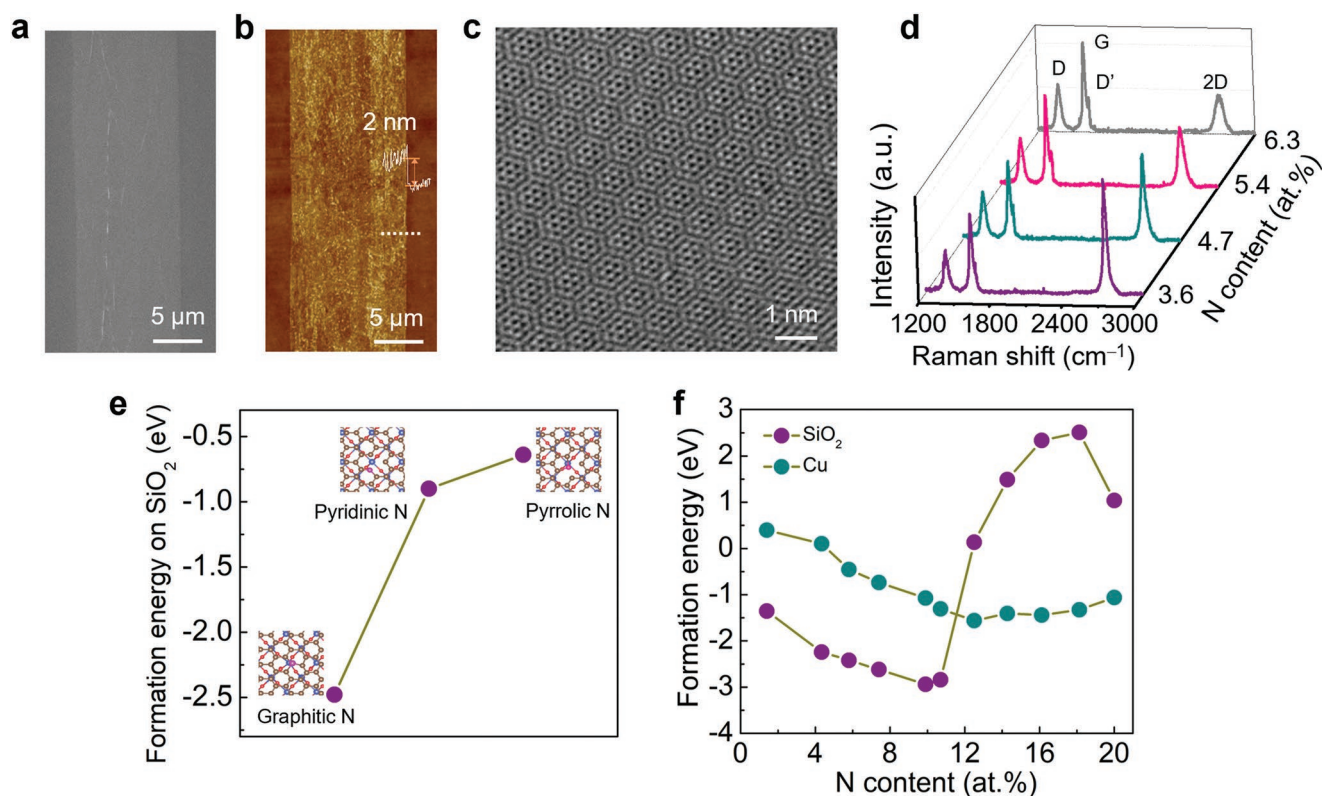


Figure 2. Controlled growth and growth mechanisms of graphitic N-doped graphene on quartz fabric. a) SEM image of a FM graphene ribbon after dissolving the inner quartz fiber. b) AFM image of a graphene ribbon. A height of ≈ 2.0 nm is measured along the white dashed line, which is the thickness of the stacked tube-like FM graphene. c) Special aberration-corrected transmission electron microscopy (AC-TEM) image of graphene obtained on quartz fiber. d) Raman spectra of graphitic N-doped graphene on quartz fabric with various substitutional levels. e, f) DFT-calculated formation energies of various types of N-doped graphene on SiO₂ (6.3 at% N) (e) and formation energies of graphitic N-doped graphene with different contents on SiO₂ and Cu foil (f).

greatly increased and the graphitic N-doped graphene forms a strong interaction with the SiO₂ substrate. On the contrary, pyrrolic and pyridinic N-doped graphene layers show weaker interactions and less electron exchanges with SiO₂ substrate, the configurations of which critically lack stability. Unanimously, a more stable graphitic-N configuration in graphene forms on quartz substrate than that on Cu substrate at the range from 1.4 to 10.7 at% N-doping levels due to the relatively lower formation energy (Figure 2f). To be more specific, after small organic molecules, such as methylammonium, ethanol methylamine, and acetonitrile decomposed at high temperature to form the stable C–N clusters, quartz fabric is one of the most energetically preferred substrates to yield graphitic N-doped graphene.^[30]

2.2. Ferromagnetism Induced by Graphitic N-Doped Graphene on Quartz Fabric

To afford an in-depth understanding of graphitic N-doping induced ferromagnetism at an atomic level, spin-polarized density functional theory (DFT) is carried out to systematically interpret the ferromagnetism of ≈ 6.3 at% graphitic-N doped graphene. Zero-field-cooled (ZFC) and field-cooled (FC) M – T curves are measured from 2 to 300 K under the applied field

$H = 0.1$ T (Figure 3a). The disparity of the two curves reveals the ordered magnetism emerging in FM graphene and magnetization sustains from 2 K up to room temperature (300 K). M – H curves are measured at 2 K under applied field from -6 to 6 T (Figure 3b). At 2 K, saturation magnification (M_s) reaches as ≈ 1.16 emu g^{−1} and the isothermal magnification of M – H curve from -0.02 to 0.02 T shows hysteresis with the typical coercivity of ≈ 79 Oe and remnant magnetization of ≈ 0.028 emu g^{−1} (inset in Figure 3b). M – H curves are measured at 300 K under applied field from -6 to 6 T (Figure 3c), which shows a saturation magnetization of ≈ 0.14 emu g^{−1} from the ferromagnetism contribution at room temperature. The isothermal magnification of M – H curve from -0.02 to 0.02 T shows hysteresis with the typical coercivity of ≈ 52 Oe and remnant magnetization of ≈ 0.008 emu g^{−1} (inset in Figure 3c) revealing a typical ferromagnetic feature. At 6.3 at% of graphitic-N, in the case of N atoms substituting C atoms at triazine-positions, the corresponding spin densities exhibit a large magnetism moment of $\approx 0.806 \mu_B$ per unit cell (Figure 3d). The density of state (DOS) demonstrates exchange coupling mediated by the conduction electrons (Figure 3e). The partial density of states (PDOS) plots exhibit that the graphitic-N induced FM state leads to a strong p_z electron peak at the Fermi level (Figure 3f). A large DOS at the Fermi level ensures ferromagnetism at a relatively high temperature. It is important to note that the graphitic-N

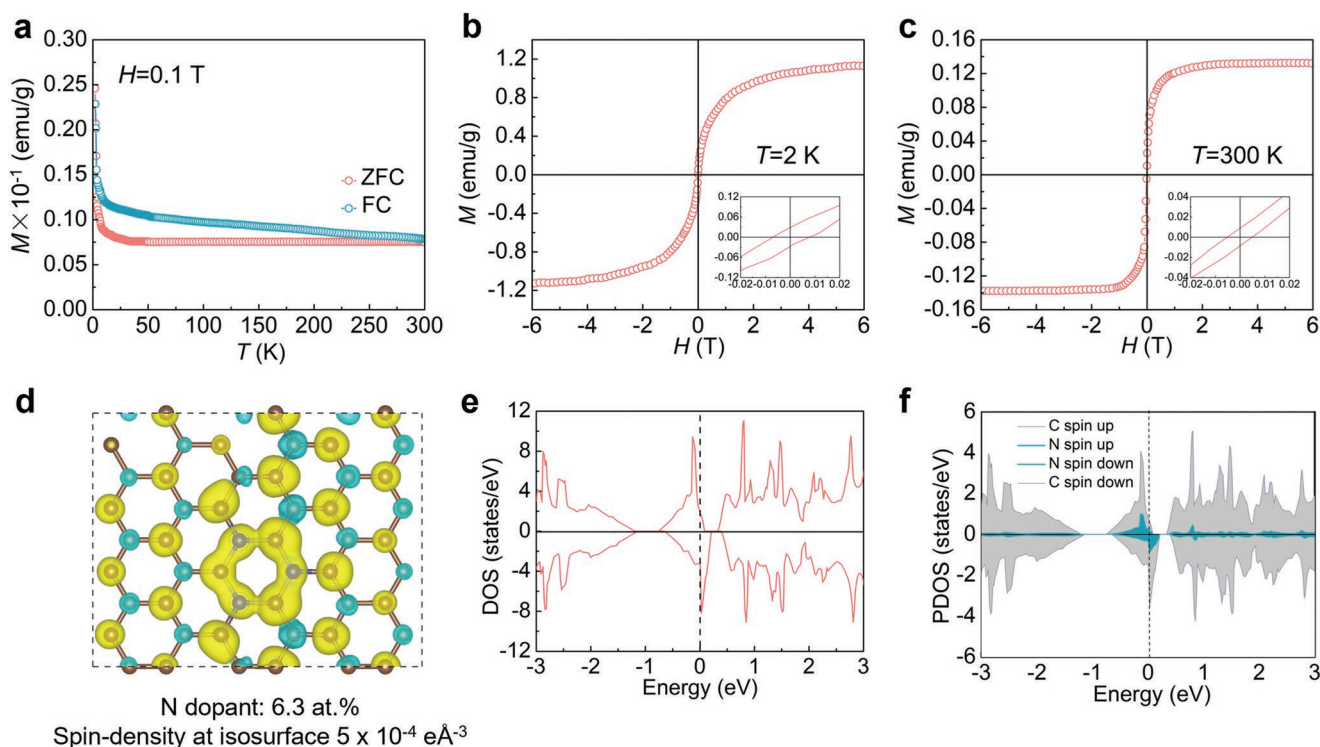


Figure 3. Magnetism measurement and DFT calculation of FM graphene. a) ZFC and FC M - T curves measured from 2 to 300 K under the applied field $H = 0.1$ T. b,c) M - H curves measured at 2 K (b) and 300 K (c). d) Top view of graphene doped with nitrogen at a concentration of 6.3 at% while spin-density plotted at isosurface $5 \times 10^{-4} \text{ e} \text{ \AA}^{-3}$. e) Density of states calculated for graphene doped with graphite N embedded in the lattices at a concentration of 6.3 at%. f) Partial densities of states calculated for graphene doped with N embedded in the lattices at a concentration of 6.3 at%.

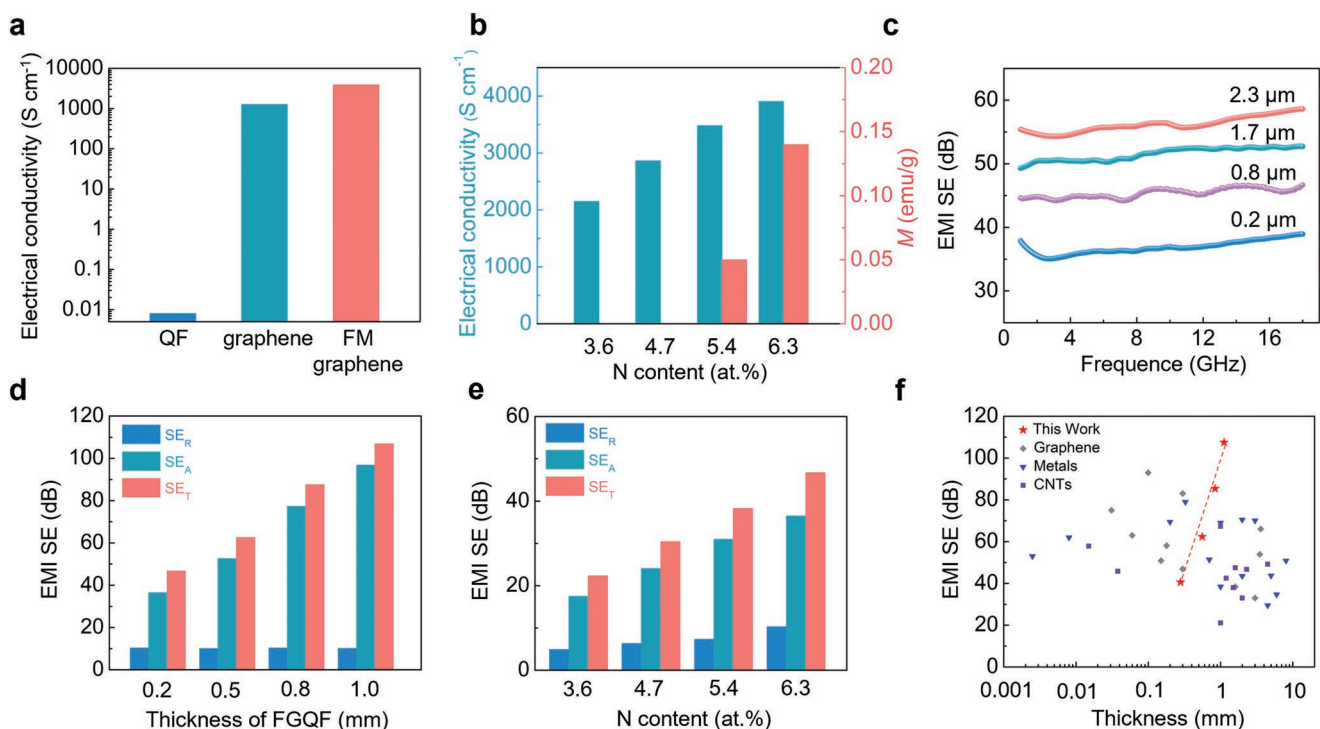


Figure 4. Electrical properties and EMI SE of FGQF. a) Electrical conductivity of QF, graphene, and FM graphene. b) Electrical conductivity and saturation magnetization at room temperature (300 K) of FM graphene with various N substitutional levels. c) EMI SE of FM graphene with various thickness in 1–18 GHz. d) SE_T , SE_R , and SE_A values of FGQF with different thickness. e) SE_T , SE_R , and SE_A values of FGQF with various N substitutional levels. f) Comparisons of EMI SE with the literature (Table S1, Supporting Information).

triggered ferromagnetism relies on the concentration and configuration of graphitic-N in graphene lattices.^[24,25]

2.3. EMI Properties of Ferromagnetic Graphene Quartz Fabric

To evaluate the EMI shielding ability, the electromagnetic properties of FM graphene and FGQF are measured in a conventional environment (see Experimental Section for more details). In general, due to free charge carriers and electric dipoles directly interact with EM field, high electrical conductivity is essential for high EMI SE. The FM graphene shows the highest electrical conductivity among experimental samples ($\approx 3906 \text{ S cm}^{-1}$), nearly three times that of undoped graphene ($\approx 1272 \text{ S cm}^{-1}$), as shown in Figure 4a and Figure S4 (Supporting Information). The electrical conductivity and saturation magnetization of FM graphene is further improved with the increasing N substitutional levels, as shown in Figure 4b. The EMI shielding properties are unambiguously confirmed that the obtained pristine FM graphene networks exhibit the extremely high EMI SE value of $\approx 58 \text{ dB}$ at the thickness of merely $\approx 2.3 \mu\text{m}$ (Figure 4c). Furthermore, A $\approx 1 \text{ mm}$ -thick FGQF in particular, demonstrates extraordinary EMI SE of $\approx 107 \text{ dB}$ over a broadband frequency (1–18 GHz) at a FM graphene coating thickness of merely 20 nm which shows obvious advantages compared with previously reported materials (Figure 4d,f; Figure S5, Supporting Information).

The total EMI SE (SE_T) comprises the contributions from reflection (SE_R), absorption (SE_A), and multiple internal reflections (SE_{MR}). In the case of high EMI SE values, multiple internal reflections are classified among the absorption because the multi-reflected waves are absorbed and transferred into heat inside the multilayers and periodic network of FGQF. The total EMI SE (SE_T) expresses as $SE_T = SE_R + SE_A$; the SE_T , SE_A , and SE_R of FGQF with different N content (at%) at a constant frequency of 8.5 GHz are shown in Figure 4e. The contribution of shielding was mainly determined by reflection SE (SE_R) and absorption SE (SE_A) combined with the reflection coefficient (R), absorption coefficient (A), and transmission coefficient (T) in FGQF. The coefficient of T is substantially low as 10^{-10} for FGQF with a thickness of $\approx 1 \text{ mm}$, indicating that more than 99.99999999% of incident EMWs are shielded by FGQF. The coefficient R is higher than A , revealing that FGQF is excellent

reflective materials (Figure S6, Supporting Information). Meanwhile, it is noted that the EMW absorption is the dominant shielding mechanism for FGQF due to the much higher SE_A than SE_R . In addition, the FGQF also shows excellent mechanical (tensile strength of 154 MPa) and anti-corrosion properties as well as flexibility (Figure S7–S11, Supporting Information), indicating the good adaptability to the complex geometry of an enclosure as well as the environmental stability.

2.4. Shielding Mechanisms of Ferromagnetic Graphene Quartz Fabric

The major EMI shielding mechanisms in the FGQF system are demonstrated in Figure 5. The EMI shielding ability of FGQF is derived from its high electrical conductivity, ferromagnetism and special woven structure. When the EMW reached the surface of FGQF, a part of them is reflected due to the interaction with the surface free charge carriers of FM graphene. The residual EMW will enter the internal FGQF because of the optimized impedance match at the interface of the air and FGQF with the superior conductive networks and will further dissipate with the specific structure of 5/2 satin and sateen weave. Subsequently, the EMW incident into FGQF will be attenuated through the multi-internal reflection in the weave superstructure and the absorption from FM graphene layers with high conductivity and magnetic permeability (Figure 5a). To be more specific, for a single FM graphene quartz fiber ($\approx 7 \mu\text{m}$ in diameter), EMW will experience the multi-reflection within the adjacent fiber arrays, and then will be attenuated by the highly effective absorption/multireflection inside the multilayers of FM graphene (Figure 5b).

Moreover, absorption loss is the major factor for electromagnetic attenuation of FGQF, which exert a profitable impact on enhancing EMW absorption. As mentioned, the multi-reflected EMW is absorbed and dissipated into heat inside the hierarchical networks of FGQF. The dielectric loss tangents $\tan \delta_e$ values show at around 2.0–3.0 which reveals a remarkable dielectric loss and high efficiency of energy dissipation of FGQF (Figure S12b, Supporting Information). It could be explained that the multiple interfaces of quartz fabric and high conductive FM graphene layers induce the large interfacial polarization and the electric dipoles resonance in FGQF. In addition,

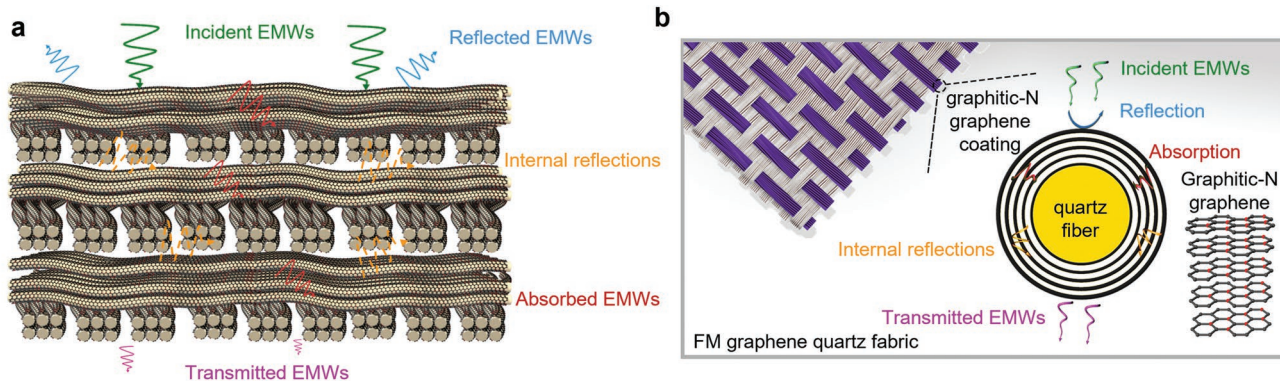


Figure 5. EMI shielding mechanisms of FGQF. a) Shielding mechanisms of FGQF. b) Shielding mechanisms of a single FM graphene quartz fiber ($\approx 7 \mu\text{m}$ in diameter) as exemplified by quartz fiber (yellow) coated by graphitic N-doped graphene layers (black).

the high magnetic loss tangents $\tan\mu_e$ value (from 0.4 to 0.6) indicates the strong magnetic loss capability of FGQF, which is conducted by hysteresis loss, resonance loss and eddy current loss (Figure S12d, Supporting Information). Therefore, the synergistic effect of hierarchical conductive networks, high- κ quartz frameworks and FM graphene multilayers greatly improves the impedance matching, dielectric loss and magnetic loss of FGQF responded over a wideband EMI shielding.

3. Conclusion

We first report the fabrication of a large-scale ($10 \times 0.5 \text{ m}^2$), flexible, and durable FGQF with ultra-broadband strong EMI shielding ability via a CVD growth process. The as-synthesized graphitic N-doped graphene coating on quartz fabric combines high conductivity and ferromagnetism to attain the synergistic effect for EMI shielding and EMWs absorption, along with the specific woven superstructure of the fabric to introduce the additional multiple reflections and multichannel absorption of EMWs. First-principles calculations reveal that graphitic N-doped graphene can trigger FM ordering and the FM graphene exhibits high magnetic responsiveness with a saturation magnetization of $\approx 0.14 \text{ emu g}^{-1}$ under 300 K, which leads to the extremely high EMI SE of $\approx 58 \text{ dB}$ at FM graphene thickness of merely $\approx 2.3 \text{ }\mu\text{m}$. With FM graphene thickness of only $\approx 20 \text{ nm}$, the $\approx 1 \text{ mm}$ -thick FGQF in particular, exhibits extraordinary EMI SE of $\approx 107 \text{ dB}$ over a broadband frequency (1–18 GHz). This work not only develops an industrial-scale, flexible, lightweight, durable, and ultra-broadband strong shielding material in potential advanced applications of flexible anti-electronic reconnaissance, antiradiation, and stealthy technologies, but also offers a paradigm of combining traditional industrial materials with the frontier 2D materials to facilitate their industrialization and commercialization in the near future.

4. Experimental Section

Continuous Batch Growth of Large-Scale FQGF: Graphitic N-doped graphene fabricated on the quartz fabric substrate with the specific 5/2 satin and sateen weave structure using ethanol, acetonitrile, and methylamine as gas feedstock by designing industrially implementable full roll to roll CVD system, which includes two winder rollers to supply and receive quartz fabrics simultaneously controlled by a stepping motor to regulate operation speed accurately. The furnace was heated to the desired growth temperature ($970\text{--}1050 \text{ }^\circ\text{C}$) under the flux of Ar (200 sccm) and H_2 (50 sccm) with a pressure of $\approx 200 \text{ Pa}$. Then, ethanol (300–800 sccm), acetonitrile (500–1000 sccm), and methylamine (1000–1500 sccm) were introduced to achieve graphitic N-doped graphene growth of different durations. After about 0.5–2 h of growth with a controllable rolling speed of $0.05\text{--}0.2 \text{ m min}^{-1}$, the CVD system was cooled rapidly under the flux of Ar and H_2 .

Computational Methods: Formation Energy: The first principles were employed to perform density functional theory (DFT) calculations within the generalized gradient approximation (GGA) by the Perdew–Burke–Ernzerhof (PBE) formulation. The projected augmented wave (PAW) potentials were chosen to depict the ionic cores and take valence electrons into account employing a plane-wave basis set with a kinetic energy cutoff of 450 eV. Partial occupancies of the Kohn–Sham orbitals were allowed using the Gaussian smearing method and a width of 0.02 eV. The k -points of $4 \times 4 \times 1$ had been used to optimize the

interface structures, which are the N-graphene/ SiO_2 and N-graphene/Cu. The electronic energy was considered self-consistent when the energy change was less than 10^{-5} eV . A geometry optimization was taken into account convergent when the energy change was less than $0.03 \text{ eV } \text{\AA}^{-1}$. Grimme's DFT-D3 methodology was employed to depict the dispersion interactions among all the atoms in adsorption models. Finally, the formation energies of N defect (E_f) were calculated as $E_f = E_{\text{total}} - nE_C - (E(\text{N}_2)m/2) - E_{\text{slab}}$, where E_{total} is the total energies of the optimized adsorbate/substrate system, E_C is the energy of a carbon atom in graphene, $E(\text{N}_2)$ is the energy of N_2 molecule, E_{slab} is the energy of Cu or SiO_2 substrate, and n represents the number of the carbon, and m stands for the number of the N atom. In addition, the U correction had been applied for Cu atom, which had been set as 3.45 eV.

Computational Methods: Magnetism Moment: All the calculations were carried out by the Vienna Ab initio Simulation Package (VASP). The interaction between valence electron and core ion was described by the PAW method. The GGA with the PBE functional was used to treat the electronic exchange-correlation interactions. To ensure high accuracy, the plane-wave cutoff energy was set to be 520 eV. In this work, the Monkhorst–Pack scheme k -points sampling was used for integration in the first Brillouin zone, which was performed with a $2 \times 3 \times 2$ Γ -point-centered Monkhorst–Pack k -point mesh per conventional 4×3 rectangular cell. The electronic density of states was calculated using the tetrahedron method with a $4 \times 6 \times 4$ k -point mesh, and the separation of the k -point mesh was smaller than 0.03 \AA^{-1} . The Bader analysis was used to get the contribution of different atoms to the ground state electron density. To avoid the interactions between periodic images, a vacuum space of 15 \AA along c directions was set for the slab. For the present calculations, the 48 carbon atoms had been employed, and spin polarization had been taken into account. The lattice parameters and the ionic positions were fully relaxed, the final force and total energy were less than $0.02 \text{ eV } \text{\AA}^{-1}$ and 10^{-4} eV for system optimizations by using a quasi-Newton algorithm.

Computational Methods: Corrosion Experiments: The FGQF specimens were tailored into a rectangular shape ($5 \text{ cm} \times 10 \text{ cm}$) and set into four environments (air, water, HCl, and NaOH) for different times (50, 100, and 150 days), respectively. Specifically, these samples were immersed in deionized water, NaOH (1 mol L^{-1}), and HCl (1 mol L^{-1}) solutions at $\approx 60 \text{ }^\circ\text{C}$ to accelerate the corrosion process. After washing with deionized water and drying, the anticorrosion efficiency was studied by the tensile strength measurement under the same conditions. Naked QF samples were tailored into the same size ($5 \text{ cm} \times 10 \text{ cm}$) and set into four environments (air, water, saturated HCl, and saturated NaOH solutions) for different times (3, 5, and 7 days), respectively.

Characterization: Optical Measurements: Raman spectra and mappings were carried out in an LabRAM HR Evolution system (Horiba, Japan) equipped with a laser excitation wavelength of 532 nm. Optical images were taken with a LV100ND microscope (Nikon). XPS spectral measurement was characterized by utilizing a Kratos Analytical Axis-Ultra spectrometer with a monochromatic Al $K\alpha$ X-ray source.

Computational Methods: TEM, AFM, and SEM Measurements: HRTEM experiments were taken with an aberration-corrected TEM FEI Titan Cubed Themis G2-300 system under 80 kV. AFM images were measured in the Dimension ICON system (Bruker, Germany) in ambient atmosphere. SEM experiments and EDS mappings were performed using FEI Quattro S (Thermo Fisher Scientific) at 2 kV.

Computational Methods: Thickness Measurement: FM graphene was etched from FGQF with 1:1 hydrofluoric acid/ethanol solution etchant. The thickness of FM graphene placed onto SiO_2 was measured with a Step profiler (BRUKER, DEKTAK XT).

Computational Methods: Magnetization Measurements: Magnetic properties of FM graphene were investigated with a physical property measurement system (PPMS DynaCool-9T) that possessed a vibrating sample magnetometer (VSM). Hysteresis loops were obtained from 2 K to 300 K under static external magnetic fields ranging from -60 to 60 kOe .

Mechanical Properties and Electrical Conductivities Measurements: The FGQF samples were tailored into a rectangle shape with a dimension of $30 \text{ mm} \times 10 \text{ mm}$ and tested by a tensile testing machine (MTS E43.104)

to obtain mechanical properties. The tensile speed was 5 mm min⁻¹ under 100 N. Adhesion evaluations of samples were using a homemade adhesion tester (refitted from a Y571 rubbing color fastness tester), the normal force applied to the eraser friction head was fixed to ≈3 N. Electrical conductivities were measured using a digital source-meters (Keithley 2400, Tektronix) at room temperature. All samples were cut into a rectangular shapes (10 mm × 25 mm), and the two ends of the samples were connected to the copper electrode with conductive silver. The voltage at the open terminal was set as 2 V.

EMI SE Measurement: The S parameters, relative complex permittivity, and permeability of the samples were measured using a vector network analyzer (Keysight N5242A) in the range of 1–18 GHz via the coaxial transmission line method in accordance with ASTM-ES-7 specification. The FGQF and FM graphene were tailored to the desired shape and the test samples (ring-shaped pieces of 7 mm outer diameter, 3 mm inner diameter, and 2 mm thickness) were prepared by impregnation with paraffin. Paraffin is the perfect supporting material as its electromagnetic parameters are very similar to those of air. The equipment was fully two-port vector calibrated prior to testing.

Theoretically, EMI SE is expressed by the Schelkunoff formalism $SE = 168 + 10 \log \left(\frac{\sigma}{f\mu} \right) + 131t\sqrt{\sigma f\mu}$, where σ [S cm⁻¹] is the electrical conductivity relative to copper, μ is the magnetic permeability, f [Hz] is the frequency, and t [m] is the thickness of the shield. Experimentally, EMI SE is measured in decibels [dB] and is expressed as $SE(\text{dB}) = 10 \log \left(\frac{P_i}{P_T} \right)$, where P_i is incoming power, P_T is transmitted power.

The reflection (R), absorption (A), and transmission (T) coefficients were calculated by the scattering parameters (S), and these three parts add up to 1. S_{11} represents the reflection loss of port 1 in the equivalent two-port network, and S_{21} represents the insertion loss of the signal from port 1 to port 2. Furthermore, SE_A and SE_R can be expressed with regard to reflection and effective absorption, which can be obtained from the R and T coefficients:

$$R = |S_{11}|^2 = |S_{22}|^2 \quad (1)$$

$$T = |S_{12}|^2 = |S_{21}|^2 \quad (2)$$

$$SE_R = 10 \log \left(\frac{1}{1-R} \right) = 10 \log \left(\frac{1}{1-|S_{11}|^2} \right) \quad (3)$$

$$SE_A = 10 \log \left(\frac{1-R}{T} \right) = 10 \log \left(\frac{1-|S_{11}|^2}{|S_{21}|^2} \right) \quad (4)$$

The dielectric complex permittivity $\epsilon_r = \epsilon'_r - i\epsilon''_r$, magnetic complex permeability $\mu_r = \mu'_r - i\mu''_r$, and tangent of dielectric loss were calculated by experimental S parameters.

Statistical Analysis: The statistical data of the tensile strength of the samples were based on corrosion experiments under different conditions (i.e., in the air, deionized water, NaOH, and HCl solutions) as a function of time. The experimental results were presented with mean ± standard deviation. Statistics were obtained from the same mechanical properties testing methods at different durations for each condition. Data were analyzed and processed using Origin software.

Supporting Information

Supporting Information is available from the Wiley Online Library or from the author.

Acknowledgements

Y.X., S.L., and K.H. contributed equally to this work. This work was supported by the National Key Basic Research Program of China (973)

(No. 2016YFA0200103), the National Natural Science Foundation of China (Nos. 51520105003, 51432002, 52062005, U1904193), The National Natural Science Foundation Committee (T2188101), Beijing National Laboratory for Molecular Sciences (BNLMS- CXTD-202001), Beijing Municipal Science & Technology Commission (Nos. Z201100008720006, Z181100004818001), Key Science and Technology Support Project of Guizhou Province (No. [2021]326) and Guizhou Provincial Science and Technology Foundation (No. [2020]1Y189). K.C. acknowledges support from the Special Program for Basic Research at the University of Henan Province (20zx010), the National Young Top-Notch Talents of Ten-Thousand Talents Program, China.

Conflict of Interest

The authors declare no conflict of interest.

Data Availability Statement

Research data are not shared.

Keywords

broadband frequency, electromagnetic interference shielding, ferromagnetic graphene quartz fabric, flexible materials

Received: April 1, 2022

Revised: May 9, 2022

Published online: June 22, 2022

- [1] Y. Yang, D. Zhu, W. Yan, A. Agarwal, M. Zheng, J. D. Joannopoulos, P. Lalanne, T. Christensen, K. K. Berggren, M. Soljačić, *Nature* **2019**, 576, 248.
- [2] M. R. Andrews, P. P. Mitra, R. deCarvalho, *Nature* **2001**, 409, 316.
- [3] D. O. Brunner, D. N. Zanche, J. Fröhlich, J. Paska, K. P. Pruessmann, *Nature* **2009**, 457, 994.
- [4] B. Zhen, M. Soljačić, *Nat. Mater.* **2016**, 15, 494.
- [5] M. Zhou, L. Ying, L. Lu, L. Shi, J. Zi, Z. Yu, *Nat. Commun.* **2017**, 8, 1388.
- [6] A. Hai, V. C. Spanoudaki, B. B. Bartelle, A. Jasanoff, *Nat. Biomed. Eng.* **2019**, 3, 69.
- [7] P. Alitalo, S. Tretyakov, *Nat. Commun.* **2012**, 3, 1213.
- [8] H. Lv, Z. Yang, B. Liu, G. Wu, Z. Lou, B. Fei, R. Wu, *Nat. Commun.* **2021**, 12, 834.
- [9] C. Pavlou, M. G. P. Carbone, A. C. Manikas, G. Trakakis, C. Koral, G. Papari, A. Andreone, C. Galiotis, *Nat. Commun.* **2021**, 12, 4655.
- [10] O. Balci, E. O. Polat, N. Kakenov, C. Kocabas, *Nat. Commun.* **2015**, 6, 6628.
- [11] K. Fan, W. J. Padilla, *Mater. Today* **2015**, 18, 39.
- [12] F. Shahzad, M. Alhabeb, C. B. Hatter, B. Anasori, S. M. Hong, C. M. Koo, Y. Gogotsi, *Science* **2016**, 353, 1137.
- [13] Z. Zeng, F. Jiang, Y. Yue, D. Han, L. Lin, S. Zhao, Y. Zhao, Z. Pan, C. Li, G. Nyström, J. Wang, *Adv. Mater.* **2020**, 32, 1908496.
- [14] Y. Fei, M. Liang, L. Yan, Y. Chen, H. Zou, *Chem. Eng. J.* **2020**, 392, 124815.
- [15] E. D. Minot, Y. Yaish, V. Sazonova, P. L. McEuen, *Nature* **2004**, 428, 536.
- [16] B. Shen, W. Zhai, W. Zheng, *Adv. Funct. Mater.* **2014**, 24, 4542.
- [17] K. S. Novoselov, A. K. Geim, S. V. Morozov, D. Jiang, M. I. Katsnelson, I. V. Grigorieva, S. V. Dubonos, A. A. Firsov, *Nature* **2005**, 438, 197.

- [18] A. A. Balandin, *Nat. Mater.* **2011**, *10*, 569.
- [19] G. Xin, T. Yao, H. Sun, S. M. Scott, D. Shao, G. Wang, J. Lian, *Science* **2015**, *349*, 1083.
- [20] Q. Wei, S. Pei, X. Qian, H. Liu, Z. Liu, W. Zhang, T. Zhou, Z. Zhang, X. Zhang, H. Cheng, W. Ren, *Adv. Mater.* **2020**, *32*, 1907411.
- [21] H. Kashani, M. Giroux, I. Johnson, J. Han, C. Wang, M. Chen, *Matter* **2019**, *1*, 1077.
- [22] W. Hu, C. Wang, H. Tan, H. Duan, G. Li, N. Li, Q. Ji, Y. Lu, Y. Wang, Z. Sun, F. Hu, W. Yan, *Nat. Commun.* **2021**, *12*, 1854.
- [23] G. Z. Magda, X. Jin, I. Hagymási, P. Vancsó, Z. Osváth, P. Nemes-Incze, C. Hwang, L. P. Biró, L. Tapasztó, *Nature* **2014**, *514*, 608.
- [24] P. Błoriski, J. Tuček, Z. Sofer, V. Mazánek, M. Petr, M. Pumera, M. Otyepka, R. Zbořil, *J. Am. Chem. Soc.* **2017**, *139*, 3171.
- [25] L. Fu, M. Di, W. Zhang, K. Zhang, Y. Wang, Y. Xu, H. Pan, Y. Zhou, Y. Du, N. Tang, *Phys. Rev. B* **2020**, *102*, 094406.
- [26] R. Shu, Z. Wan, J. Zhang, Y. Wu, Y. Liu, J. Shi, M. Zheng, *ACS Appl. Mater. Interfaces* **2020**, *12*, 4689.
- [27] Y. Zhang, Y. Huang, T. Zhang, H. Chang, P. Xiao, H. Chen, Z. Huang, Y. Chen, *Adv. Mater.* **2015**, *27*, 2049.
- [28] K. S. Kim, Y. Zhao, H. Jang, S. Y. Lee, J. M. Kim, K. S. Kim, J. Ahn, P. Kim, J. Choi, B. H. Hong, *Nature* **2009**, *457*, 706.
- [29] L. Gao, G. Ni, Y. Liu, B. Liu, A. H. C. Neto, K. P. Loh, *Nature* **2014**, *505*, 190.
- [30] L. Lin, J. Li, Q. Yuan, Q. Li, J. Zhang, L. Sun, D. Rui, Z. Chen, K. Jia, M. Wang, Y. Zhang, M. H. Rummeli, N. Kang, H. Q. Xu, F. Ding, H. Peng, Z. Liu, *Sci. Adv.* **2019**, *5*, 8337.